Localizing Low-Grade Heat Using Hybrid Photonic-Phononic Materials

Elliot K. Beutler,[†] Vishal Kumar,[‡] Gordon H. K. Duddy,[‡] Marc R. Bourgeois,[†] Bernadeta R. Srijanto,[¶] Jordan A. Hachtel,[¶] David J. Masiello,[*,†] and Jon P. Camden[*,‡]

†*Department of Chemistry, University of Washington, Seattle, WA 98195, United States*

‡*Department of Chemistry, University of Notre Dame, Notre Dame, Indiana 46556, United States*

¶*Center for Nanophase Materials Sciences, Oak Ridge National Laboratory, Oak Ridge, Tennessee 37831, United States*

E-mail: masiello@uw.edu; jon.camden@nd.edu

Abstract

Creating next-generation devices capable of transducing waste heat into useful work will require building blocks designed to direct low-grade thermal energy at length scales well below the diffraction limit. Characterizing thermally-induced energy transfer at the nanoscale, however, is a formidable task due to the simultaneous demand of high spatial and spectral resolution at infrared energies. Leveraging recent advancements in electron energy loss (EEL) and gain (EEG) spectroscopy, we reveal that individual nanostructures can concentrate energy by resonant thermal excitation of their photonic Fabry-Pérot modes. Specifically, we show that the spatially localized gain signal increases upon *in situ* heating. Theoretical modeling elucidates the mechanism for

these observations by showing that a Purcell enhancement in the local photonic density of states drives the increased rate of infrared energy transfer from the ambient environment to each nanostructure.

Waste heat generation is an unavoidable consequence of human activity across all sectors and new strategies for harnessing this lost energy are urgently needed if we are to meet global climate goals and support sustainable development.[1] It is estimated, for example, that up to 70% of global primary energy consumption is lost to the surrounding environment as waste heat, with low-grade heat (< 100 °C) constituting the largest fraction ($> 60\%$) of the lost energy.[2] This inefficiency has stimulated intensive research efforts into waste heat remediation[3] but effective use of low-grade heat remains an formidable challenge. To date, thermoelectric devices have dominated the recovery of low-grade heat;[4–10] unfortunately, state-of-the-art thermoelectrics often employ toxic and rare-earth metals, limiting their sustainability and accessibility.[11] Additionally, despite recent improvements, efficiency gains have plateaued[12] and large barriers to commercial devices remain.[13] There is, therefore, an urgent need to develop waste heat recovery systems, built using sustainable materials, that can be easily integrated into existing technologies. Towards this end, harnessing near-field effects to improve the conversion efficiencies of photovoltaics and thermophotovoltaics is an exciting approach vector.[14] Infrared (IR) active photonic nanostructures in particular present an exciting platform to localize and direct low-grade heat both spatially and spectrally as IR resonances are easily accessible via thermal excitation.[15–19]

At length scales much smaller than the associated wavelengths of IR radiation ($\ll 1$ μm), contributions from near-field evanescent photons to the energy density are many orders of magnitude greater than those of their propagating counterparts.[20,21] Therefore, the evanescent fields localized around heated IR-active nanostructures show promise as potential sources of harvestable thermal energy and potential conduits for controllable nanoscale heat transfer. Due to recent advances in electron energy monochromation and aberration correction in the electron microscope,[22] a broad class of thermally active material responses such as

collective phononic and photonic excitations are now accessible to spectral and spatial mapping via electron energy loss (EEL)[23,24] and electron energy gain (EEG)[25–30] spectroscopies performed inside a scanning transmission electron microscope (STEM). Far exceeding the diffraction-limited resolution of light-based measurements, such STEM spectroscopies are ideal for exploring the modes of thermal energy transfer within composite nanostructures at their native length scales.

In this Letter, we demonstrate the capacity for gold nanowires, supporting thermally active photonic Fabry-Pérot (FP) resonances, to spatially focus the IR radiation generated by their supporting dielectric substrate upon heating. In contrast to previous work using coupled nanostructures to achieve one-way flow of optical energy[31,32] or the nanolocalization of thermal gradients,[33–35] here we investigate the potential for hybrid photonic-phononic materials to locally enhance the rate of IR energy extraction from their ambient environment. Specifically, we measure the temperature dependent and spatially resolved inelastic electron scattering from individual nanowires immobilized on an *in situ* protochip heating holder. A clear enhancement in the EEG scattering probability is observed as the thermal occupation of the phononic and photonic modes of the substrate-nanowire system is increased. A theoretical model to quantify the nanowire's potential to concentrate IR energy in the presence of a thermally excited substrate is developed. The resulting model shows that the enhanced gain signal can be understood as a generalized Purcell enhancement effect with the STEM electrons directly probing the local occupation of the photonic density of states.

Fig. 1a displays an SEM image of the gold nanowire structures which support thermally active FP modes that can be tuned throughout the IR by changing the nanowire length.[36–38] The nanowires were prepared on a silicon nitride (SiN) membrane that was subjected to Ohmic heating (Fig. 1b) while the STEM electron beam was used for spectroscopic characterization (Fig. 1c). A detailed description of the nanowire fabrication and STEM characterization can be found in the Supporting Information (SI). Fig. 1d displays a point EEL spectrum measured at the end of a 2 μm nanowire (black) deposited on a SiN sub-

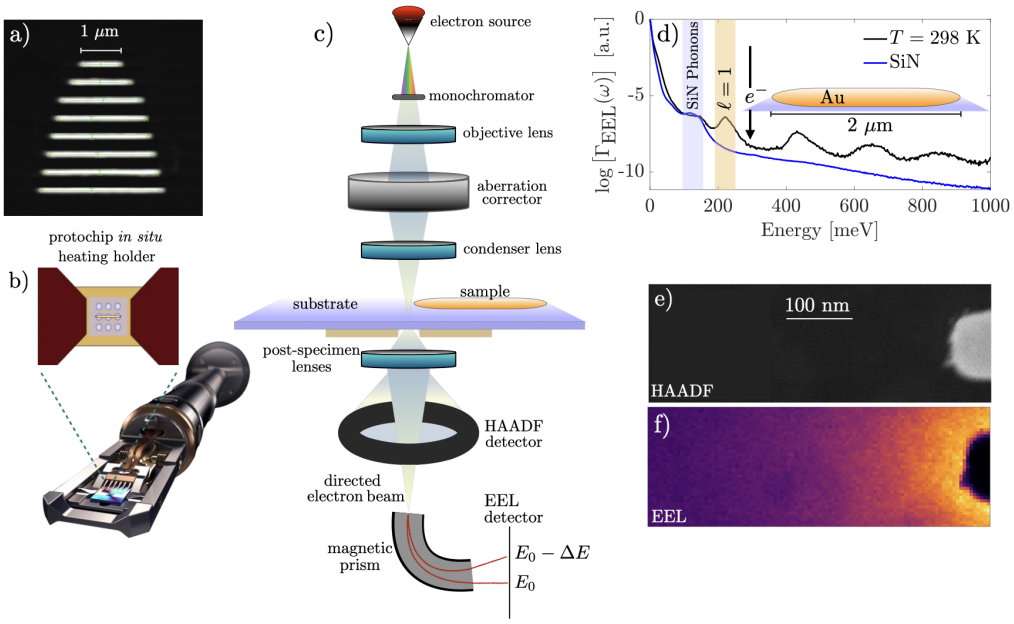

Figure 1: Thermally-assisted inelastic-electron scattering measurements. a) A collection of gold nanowires ranging in length from $1-3$ μm are fabricated on a protochip membrane. b) A heated protochip holder allows for *in situ* heating of the nanowire-substrate sample. c) EEL and EEG spectroscopy performed in a STEM allows for nanoscale imaging of the thermal gain. d) EEL spectrum obtained at the end of a nanowire deposited on a SiN substrate, highlighting (gold) the $\ell = 1$ FP resonance and (blue) the phononic resonances of the dielectric substrate e) HAADF image of the tip of a 2 μm gold nanowire. f) Spectrum image of the inelastic scattering intensity at the $\ell = 1$ FP mode energy (220 meV), demonstrating how STEM EELS reveals the spatial localization of the photonic density of states.

strate (in an aloof configuration with a 10 nm impact parameter). The resulting energy loss signal is plotted on a logarithmic scale and demonstrates a progression of IR FP resonances oriented along the nanowire's long axis, with the lowest order $\ell = 1$ FP mode excited around 220 meV (gold shaded region). Additionally, an EEL spectrum of the SiN substrate is recorded far from any nanowires (blue). The SiN substrate hosts a collection of bulk and surface phonon modes which are probed by the electron in a penetrating configuration with the surface phonon mode energies contained within the shaded blue region. Included as an inset is a schematic of the composite nanowire-substrate assembly. The high angle annular dark field (HAADF) image in Fig. 1e displays the region of space around the nanowire tip probed by the electron current. Fig. 1f is an EEL spectrum image obtained at the $\ell = 1$ FP mode energy, reflecting the spatial profile of the optical cavity mode which is largest at the ends of the nanowire.

The experimental anti-Stokes (Γ_{EEG}) and Stokes (Γ_{EEL}) scattering signals are plotted in Fig. 2a as a function of temperature for two different nanowire lengths, 4 μm and 2 μm. These lengths were chosen such that the $\ell = 1$ (dipolar) mode of the 2 μm nanowire and the $\ell = 2$ (quadrupolar) mode of the 4 μm are approximately the same energy ($\sim$ 220 meV), allowing for the investigation of degenerate bright and dark modes, i.e., those that are coupled or not coupled to the far field, respectively. Given the different spatial dependencies of these modes, the aloof electron beam is placed either adjacent to the nanowire's end or center respectively, represented by the blue dots in the insets. Regions of the spectra corresponding to anti-Stokes scattering are plotted as negative energies with respect to the zero loss peak (ZLP) at 0 meV. This signal is the thermally stimulated EEG, where the electron probe has gained energy from the thermally-occupied modes of the composite structure. The positive energies relative to the ZLP represent the thermally-assisted Stokes or EEL signal, where the electron probe has resonantly deposited its own kinetic energy into the target's thermally occupied surface modes.

Fig. 2b examines how the EEG signal from the $\ell = 1$ FP resonance of the 2 μm nanowire

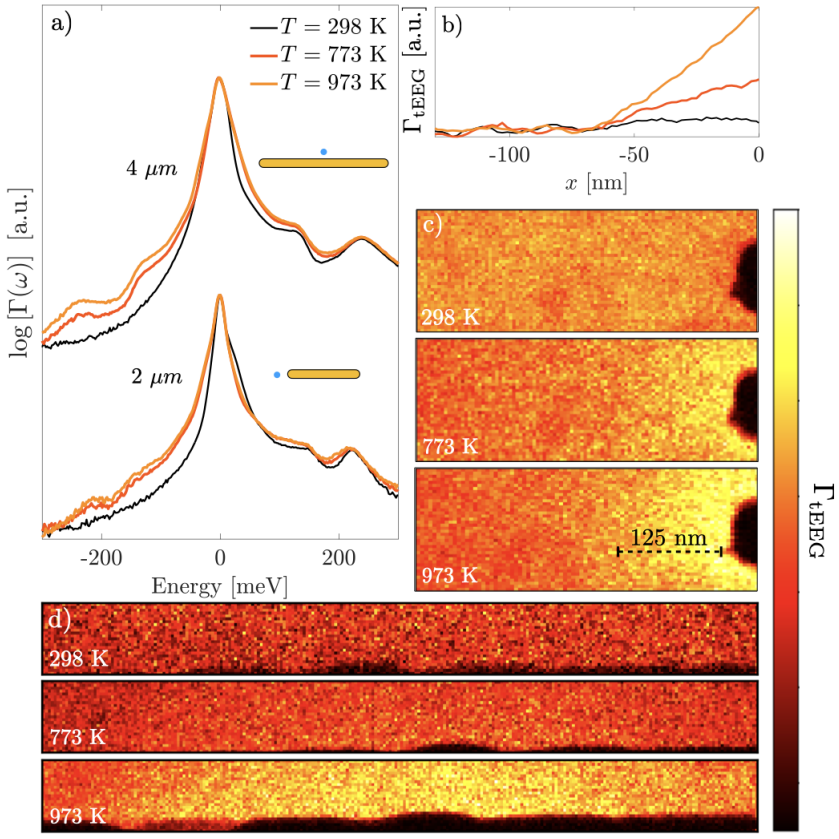

Figure 2: Thermally-assisted inelastic electron scattering processes. a) EEL and EEG point spectra for a 2 μm (lower) and a 4 μm (upper) long gold nanowire for temperatures between $298 - 973$ K. The point spectra are acquired at the beam positions indicated by the blue dots in the inset and are normalized to the ZLP. The gain signal (negative energy values) increases with increasing temperature for both the dipolar (2 μm) and quadrupolar (4 μm) FP modes. b) Plotting the EEG signal as a function of distance from the rod end ($\ell = 1$ surface mode energy of the 2 μm nanowire) illustrates the increased spatial localization with increased temperature. c) Temperature dependent and spatially resolved EEG spectrum images obtained at the $\ell = 1$ FP mode energy (-220 meV) of the 2 μm wire. d) Temperature dependent and spatially resolved EEG spectrum images obtained at the $\ell = 2$ FP mode energy (-220 meV) near the center the 4 μm wire.

varies as a function of distance from the wire end. A clear increase in thermal occupation is indicated by the growing magnitude of the anti-Stokes scattering intensity as the temperature is increased. Fig. 2c presents a series of EEG spectrum images evaluated at the same $\ell = 1$ FP resonance of the nanowire, demonstrating an increasing probability for the electron probe to extract thermal energy from the nanowire-substrate system when it is focused near the nanowire tip as the system temperature is increased from $298 - 973$ K. Spectrum images of the $\ell = 2$ FP mode evaluated near the center of the 4 μm nanowire are plotted in Fig. 2d over the same temperature range, again demonstrating an increase in the thermally assisted gain process and the companion spatial concentration of thermal energy into the near-field. Interestingly, these data illustrate how optically dark FP modes can be significantly populated via thermal excitation and in accordance with Bose-Einstein statistics.[39]

The optical response of a material is fully captured by its induced Green's function and its closely related local density of states (LDOS),[40–42] where the LDOS measures the availability of electromagnetic modes at a particular point in space per unit frequency.[43] The spatial and spectral characteristics of each mode can be dramatically altered when coupled to their local environment,[44] such as a neighboring nanostructure,[32,45,46] an optical cavity,[47,48] or an underlying substrate.[17,37,49] The thermally dressed Stokes $\Gamma_{\mathrm{EEL}}(\omega)$ and anti-Stokes $\Gamma_{\mathrm{EEG}}(\omega)$ scattering signals are related to the spontaneous Stokes scattering $\Gamma^0_{\mathrm{EEL}}(\omega)$ at $T = 0$ K by

$$\Gamma_{\mathrm{EEL}}(\omega) = [n(\omega) + 1]\,\Gamma^0_{\mathrm{EEL}}(\omega) \tag{1}$$

$$\Gamma_{\mathrm{EEG}}(\omega) = n(\omega)\Gamma^0_{\mathrm{EEL}}(\omega), \tag{2}$$

via the Bose-Einstein statistical factor $n(\omega) = [\exp(\hbar\omega/kT) - 1]^{-1}$.[50,51] The ratio of the EEG and EEL signals at a common temperature yields the Boltzmann distribution, $\Gamma_{\mathrm{EEG}}/\Gamma_{\mathrm{EEL}} = \exp(-\hbar\omega/kT)$, illustrating that the gain and loss processes obey the principle of detailed balance when the STEM electron probes the system in a state of static thermal equilibrium.

This statistical relation between the thermally assisted EEG and EEL observables has been recently employed for performing high resolution thermometry measurements,[25,26] allowing for a mapping of nanoscale temperature distributions.

Beyond nanoscopic thermometric measurements, the EEG signal may be utilized to spatially characterize the modes of IR-mediated thermal energy transport in composite nanostructures at their native nanometer length scales. To make this point explicit, the spontaneous inelastic scattering probability per unit energy can be written as[51]

$$\begin{aligned}\Gamma^{0}_{\mathrm{EEL}}(\omega) &= -\frac{1}{\pi\hbar^{2}}\int d\mathbf{x}d\mathbf{x}'\ \mathrm{Im}\left[\rho^{*}(\mathbf{x},\omega)G(\mathbf{x},\mathbf{x}';\omega)\rho(\mathbf{x}',\omega)\right] \\ &= \left(\frac{e}{\hbar v}\right)^{2}\omega\,\varrho(\mathbf{R}_{0},q_{z}=\omega/v,\omega),\end{aligned} \tag{3}$$

in the quasistatic approximation, which is valid in the low frequency limit where target material dimensions are much smaller than the effective wavelength at IR energies. Considering a tightly focused STEM electron in Eq. (3), the relevant current distribution $\mathbf{J}(\mathbf{x},\omega) = -e\hat{\mathbf{z}}\delta(\mathbf{R}-\mathbf{R}_{0})e^{i\omega z/v}$ and associated charge density $\rho(\mathbf{x},\omega) = (-i/\omega)\nabla\cdot\mathbf{J}(\mathbf{x},\omega) = (e/v)\delta(\mathbf{R}-\mathbf{R}_{0})e^{i\omega z/v}$, with $\mathbf{x} = (\mathbf{R}_{0},z)$ and impact parameter $\mathbf{R}_{0}$, render the EEL probability directly proportional to the target's Green's function $G(\mathbf{x},\mathbf{x};\omega)$.[52] This important result provides a direct connection between the inelastic scattering signal $\Gamma^{0}_{\mathrm{EEL}}(\omega)$ and the target's photonic LDOS $\varrho(\mathbf{x},\omega) = -(\pi\omega)^{-1}\,\mathrm{Im}[G(\mathbf{x},\mathbf{x};\omega)]$. More specifically, $\Gamma^{0}_{\mathrm{EEL}}(\omega)$ (and $\Gamma_{\mathrm{EEL}}(\omega)$ and $\Gamma_{\mathrm{EEG}}(\omega)$) are direct measures of the LDOS $\varrho(\mathbf{R}_{0},q_{z}=\omega/v,\omega)$ expressed in reciprocal q_{z}-space conjugate to the electron's trajectory along the z-axis.[42] Taking Eqs. (2) and (3) together illustrates that the STEM electron can directly probe the temperature dependent population of the target's states due to the statistical weighting of the Bose-Einstein distribution.

To elucidate the temperature dependent experimental measurements, the nanowire and substrate are theoretically modeled as an interacting sphere-substrate system where the substrate is taken to be semi-infinite in depth. As will be demonstrated, approximating the nanowire by a nanosphere and the finite thickness substrate as semi-infinite captures

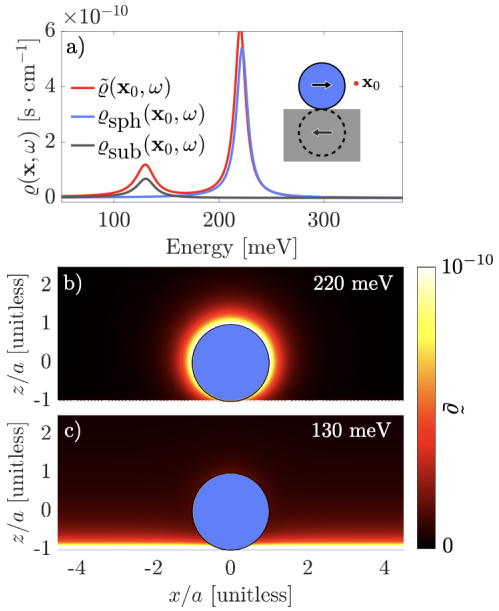

Figure 3: Spectral and spatial dependence of the phononic-photonic model system LDOS. a) LDOS spectrum of the composite system (red) and of the individual sphere (blue) and substrate (gray) demonstrating resonance features at the free substrate ($\sim$ 130 meV) and free sphere ($\sim$ 220 meV) energies. All spectra are evaluated at the point $\mathbf{x}_0 = (1.1a, 0, 0)$, where the sphere's $\ell = 1, m = \pm 1$ FP mode oriented parallel to the substrate surface is excited. The slight redshift of the dressed sphere's mode energy is due to interaction with the induced charge distribution it generates on the substrate surface. b) Evaluating the LDOS of the composite system at 220 meV illustrates a spatial localization of the FP mode density to the region surrounding the spherical particle surface. c) Evaluating the LDOS at 130 meV illustrates a localization of the phononic mode density along the the semi-infinite dielectric interface in the vicinity of the particle.

the essential physics of the experimental system. These simplifications make the model analytically tractable and thus allow us to extract more detailed physical insights. Solving the resulting dynamical equations (SI) produces a set of mixed-mode Green's functions of the coupled photonic-phononic system along with its LDOS $\widetilde{\varrho}(\mathbf{x},\omega)$ in the dipole limit (SI). Plotted in Fig. 3a is the composite LDOS spectrum evaluated at the position $\mathbf{x}_0 = (1.1a, 0, 0)$ and characterized by two resonance peaks (red curve). The ~ 130 meV feature is associated with the sphere-dressed substrate phononic response, while the ~ 220 meV feature is due to the response of the substrate-dressed sphere $\ell = 1$, $m = \pm 1$ FP mode. A comparison is made to the free space sphere (blue curve) and substrate (gray curve) LDOS spectra. Slight differences in the dressed mode energies of the composite LDOS evaluated at $\mathbf{x}_0$ arise due to coupling of the $\ell = 1, m = \pm 1$ FP surface mode with its generated image on the substrate. As a result, the dressed FP mode is shifted to a slightly lower energy than the free sphere. In Figs. 3b and 3c, spectrum images of the LDOS in the vacuum region above the SiN substrate are evaluated at the free sphere and substrate mode energies, showing a strong localization of the LDOS to the sphere's surface when evaluated at the sphere resonance energy (220 meV) and to the substrate surface when it is evaluated near the substrate resonance energy (130 meV). To produce the LDOS in Fig. 3, a least-squares fitting routine is employed to the experimental EEL data in Fig. 1d to extract the dielectric parameters of a Lorentz oscillator model, which is then applied in constructing the free-space polarizability of the spherical particle. Fit parameters for the underlying SiN substrate are extracted from ellipsometric data.[53] With $\widetilde{\varrho}(\mathbf{x},\omega)$ defined for the composite system, a calculation of both spontaneous and thermally dressed inelastic electron scattering in terms of the LDOS of the vacuum half-space is now straightforward with the use of Eqs. (1), (2), and (3).

Measurement of a generalized Purcell enhancement $F(\mathbf{R}_0,\omega)$ can be evaluated as a ratio between the LDOS of the composite system $\widetilde{\varrho}$ at point $\mathbf{R}_0$ and the LDOS of the isolated substrate ϱ_{sub},[54] where the proximity of the substrate to the optical modes of the nanowire cavity leads to an increase in the photonic density of states. Because the total inelastic

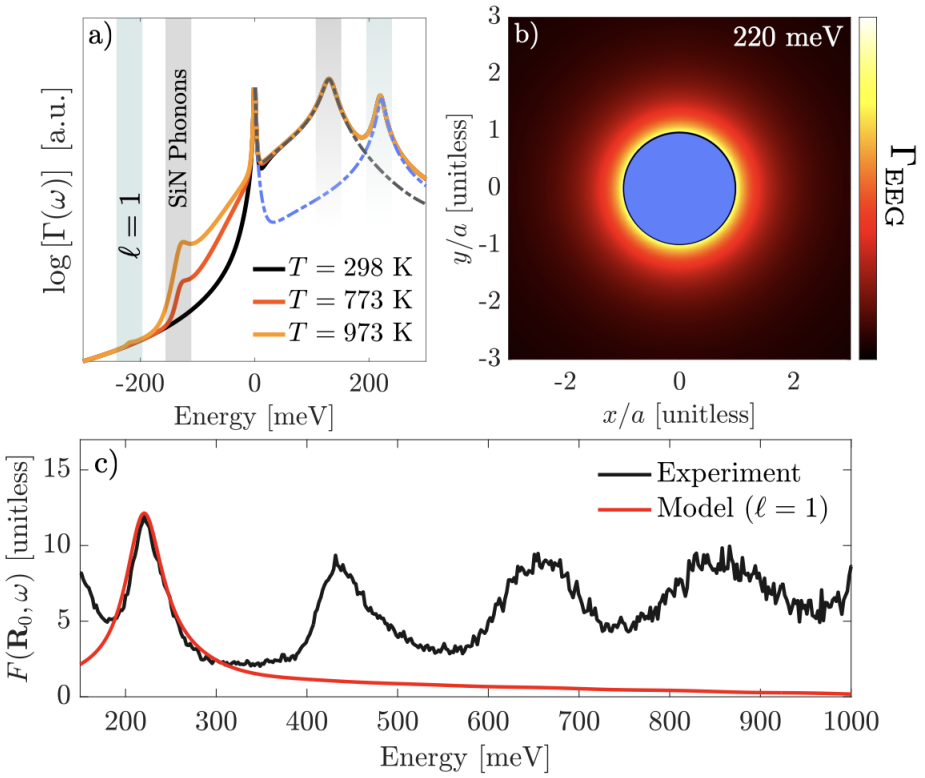

Figure 4: Theoretically determined spectral responses of the coupled photonic-phononic system from Fig. 3. a) Inelastic scattering signal produced by the particle-substrate system with increasing temperature $T = 298 - 973$ K, considering a sphere with radius $a = 50$ nm, placed on top of a semi-infinite SiN dielectric substrate, and calculated with the aid of Eqs. (1), (2), (3), and the mixed-mode Green's functions (SI). b) EEG spectrum image evaluated at the $\ell = 1$ FP resonance energy (-220 meV). c) Comparison of the Purcell enhancement $F(\mathbf{R}_0, \omega) = \Gamma(\omega)/\Gamma_{\mathrm{sub}}(\omega)$ from the experimentally derived data (black) and analytical particle-substrate model (red). Model spectra in panels a,c are evaluated at $\mathbf{R}_0 = (1.1a, 0)$, while the experimental point spectrum in panel c is measured 10 nm from the nanowire tip.

electron scattering signal $\Gamma(\omega)$, which accounts for both EEL and EEG processes, is directly proportional to the LDOS, the enhancement $F(\mathbf{R}_0, \omega)$ can also be measured from the ratio of the composite system's scattering probability to that of the bare substrate as

$$\begin{aligned} F(\mathbf{R}_0, \omega) &= \frac{\widetilde{\varrho}(\mathbf{R}_0, q_z = \omega/v, \omega)}{\varrho_{\text{sub}}(\mathbf{R}_0, q_z = \omega/v, \omega)} \\ &= \frac{\Gamma(\omega)}{\Gamma_{\text{sub}}(\omega)}. \end{aligned} \tag{4}$$

As shown in the model calculations presented in Fig. 4, the resulting enhancement indicates that the presence of the nanowire allows for a means of efficient thermal energy transfer from the heated substrate to the high quality factor FP modes localized in the vicinity of the nanowire. Substituting the mixed-mode Green's functions for the interacting sphere $\widetilde{G}_{\text{sph}}$ and substrate $\widetilde{G}_{\text{sub}}$ (SI) into Eq. (3), the resulting spontaneous inelastic scattering probability $\Gamma^0_{\text{EEL}}(\omega)$ is finally used in tandem with Eqs. (1) and (2) to produce the thermally dressed Stokes and anti-Stokes scattering signals over the same temperature range as the experimentally acquired signals (Fig. 4a). To account for the ZLP in the experimentally acquired signal, a Lorentzian function is included at 0 meV, with a spectral width of 10 meV. Because $\widetilde{G}_{\text{sph}}$ and $\widetilde{G}_{\text{sub}}$ are only defined in the vacuum half-space, the integrated path traversed by the electron is restricted to the region of space $z, z' > 0$, and the integration is performed numerically over a trajectory length of ~ 5000 nm ($z, z' = 100a \rightarrow -0.99a$). Fig. 4b is a computed spectrum image of the EEG signal at the $\ell = 1$ FP mode energy, and Fig. 4c is a measure of the Purcell factor $F(\mathbf{R}_0, \omega)$ derived from both the experimental (black) and numerically (red) acquired data for the inelastic scattering signal of the isolated substrate and the composite particle-substrate system, utilizing Eq. (4).

Taken together, these results show that the $\ell = 1$ FP mode of the nanowire exhibits a Purcell enhancement of $F \approx 12$. This means that there is a 12-fold increase in the efficiency of thermal energy transfer to the probing electron due to the presence of the gold nanowire as compared to the bare SiN substrate alone, i.e., $\Gamma(\mathbf{R}_0, \omega) \approx 12 \cdot \Gamma_{\text{sub}}(\omega)$ for points $\mathbf{R}_0$ in the

vicinity of the the nanowire. Our model further shows that the increased inelastic scattering signal is directly correlated with the increased photonic LDOS in the nanowire's immediate vicinity as reported by the Purcell enhancement metric $F(\mathbf{R}_0, \omega)$. This order of magnitude increase in the LDOS is indicative of an enhancement in the rate of thermal energy transfer from the delocalized heated substrate to its local environment where the thermal energy may be efficiently harvested.

In conclusion, inelastic electron scattering spectroscopy was used to measure the spatially-dependent increase in the local density of states that results from thermal population of the hybrid modes of a coupled nanowire-substrate system at elevated temperature. The electron probe provides deeply sub-diffraction-limited spatial resolution, revealing the near-field behavior of the thermally excited IR FP mode resonances inherent to each nanowire at their native length and energy scales. Thermal excitation of the FP modes was facilitated by resistive heating of the SiN substrate, stimulating phononic excitations that couple to the IR modes of the nanowire. The influence of incrementally increasing the system temperature was observed in the measured EEL and EEG signals, where an increase in inelastic scattering intensity coincided with an increase in system temperature, as a consequence of Bose-Einstein statistics. Companion theoretical modeling was used to elucidate the mechanism for these observations based on a Purcell enhancement in the composite system's LDOS. Taken together, this work provides a guide to the design of devices capable of efficiently harvesting and directing ambient thermal energy at the nanoscale such as the transduction of delocalized mechanical energy in the form of phonons into localized optical excitations.

Acknowledgement

This work was supported by the Air Force Office of Scientific Research (AFOSR) under Award FA9550-21-1-0282 (E.K.B., V.K., G.H.K.D., M.R.B., D.J.M., J.P.C.). Any opinions, findings, and conclusions or recommendations expressed in this material are those of the

author(s) and do not necessarily reflect the views of the United States Air Force. All STEM experiments and nanofabrication were conducted at the Center for Nanophase Materials Sciences, which is a DOE Office of Science User Facility (B.R.S., J.A.H.). This research was conducted, in part, by using instrumentation within ORNL's Materials Characterization Core provided by UT-Battelle, LLC, under Contract DE-AC05-00OR22725 with the DOE, and sponsored by the Laboratory Directed Research and Development Program of Oak Ridge National Laboratory, managed by UT-Battelle, LLC, for the U.S. Department of Energy.

Supporting Information Available

Detailed description of Au nanowire synthesis and deposition on top of a SiN substrate and *in situ* protochip heating holder for variable temperature control under EEL and EEG spectroscopic measurements. Additionally an in-depth derivation of the mixed-mode Green's functions and the corresponding density of states in the dipole coupling limit is provided as a means of modeling the particle substrate system interrogated by fast electrons.

References

(1) Cullen, J. M.; Allwood, J. M. Theoretical efficiency limits for energy conversion devices. *Energy* **2010**, *35*, 2059–2069.

(2) Forman, C.; Muritala, I. K.; Pardemann, R.; Meyer, B. Estimating the global waste heat potential. *Renewable and Sustainable Energy Reviews* **2016**, *57*, 1568–1579.

(3) Jouhara, H.; Khordehgah, N.; Almahmoud, S.; Delpech, B.; Chauhan, A.; Tassou, S. A. Waste heat recovery technologies and applications. *Thermal Science and Engineering Progress* **2018**, *6*, 268–289.

(4) Hu, S.; Ren, Z.; Djurišić, A. B.; Rogach, A. L. Metal halide perovskites as emerging thermoelectric materials. *ACS Energy Letters* **2021**, *6*, 3882–3905.

(5) Wang, T.; Xu, X.; Li, W.; Li, Y.; Liu, Q.; Li, C.; Shan, C.; Li, G.; Shi, T.; Kyaw, A. K. K. Simultaneous Enhancement of Thermoelectric Power Factor and Phase Stability of Tin-Based Perovskites by Organic Cation Doping. *ACS Applied Energy Materials* **2022**, *5*, 11191–11199.

(6) Zhang, D.; Lim, W. Y. S.; Duran, S. S. F.; Loh, X. J.; Suwardi, A. Additive manufacturing of thermoelectrics: emerging trends and outlook. *ACS Energy Letters* **2022**, *7*, 720–735.

(7) Zhang, D.; Lim, X. J. G.; Li, X.; Saglik, K.; Solco, S. F. D.; Tan, X. Y.; Leow, Y.; Zhai, W.; Tan, C. K. I.; Xu, J. et al. 3D-Printed Porous Thermoelectrics for In Situ Energy Harvesting. *ACS Energy Letters* **2022**, *8*, 332–338.

(8) Tang, J.; Pai, Y.-H.; Liang, Z. Strategic insights into semiconducting polymer thermoelectrics by leveraging molecular structures and chemical doping. *ACS Energy Letters* **2022**, *7*, 4299–4324.

(9) Cao, J.; Dong, J.; Saglik, K.; Zhang, D.; Solco, S. F. D.; You, I. J. W. J.; Liu, H.; Zhu, Q.; Xu, J.; Wu, J. et al. Non-equilibrium strategy for enhancing thermoelectric properties and improving stability of AgSbTe2. *Nano Energy* **2023**, *107*, 108118.

(10) Shi, L.; Li, D.; Yu, C.; Jang, W.; Kim, D.; Yao, Z.; Kim, P.; Majumdar, A. Measuring thermal and thermoelectric properties of one-dimensional nanostructures using a microfabricated device. *Journal of Heat and Mass Transfer* **2003**, *125*, 881–888.

(11) Caballero-Calero, O.; Ares, J. R.; Martín-González, M. Environmentally friendly thermoelectric materials: High performance from inorganic components with low toxicity and abundance in the earth. *Advanced Sustainable Systems* **2021**, *5*, 2100095.

(12) He, J.; Tritt, T. M. Advances in thermoelectric materials research: Looking back and moving forward. *Science* **2017**, *357*, eaak9997.

(13) Yan, Q.; Kanatzidis, M. G. High-performance thermoelectrics and challenges for practical devices. *Nature Materials* **2022**, *21*, 503–513.

(14) Pascale, M.; Giteau, M.; Papadakis, G. T. Perspective on near-field radiative heat transfer. *Applied Physics Letters* **2023**, *122*, 100501.

(15) Tang, L.; DeSutter, J.; Francoeur, M. Near-field radiative heat transfer between dissimilar materials mediated by coupled surface phonon-and plasmon-polaritons. *ACS Photonics* **2020**, *7*, 1304–1311.

(16) Olafsson, A.; Busche, J. A.; Araujo, J. J.; Maiti, A.; Idrobo, J. C.; Gamelin, D. R.; Masiello, D. J.; Camden, J. P. Electron beam infrared nano-ellipsometry of individual indium tin oxide nanocrystals. *Nano Letters* **2020**, *20*, 7987–7994.

(17) Beutler, E. K.; Lagos, M. J.; Masiello, D. J. Infrared surface phonon nanospectroscopy of an interacting dielectric-particle–dielectric-substrate dimer using fast electrons. *Physical Review B* **2021**, *103*, 165418.

(18) Kumar, V.; Rossi, A. W.; Lawson, Z. R.; Neal, R. D.; Hachtel, J. A.; Neretina, S.; Masiello, D. J.; Camden, J. P. Infrared Near-Field Spectroscopy of Gold Nanotriangle Fabry-Pérot Resonances. *Journal of Physical Chemistry C* **2023**, *127*, 6777–6784.

(19) Yokoyama, T.; Dao, T. D.; Chen, K.; Ishii, S.; Sugavaneshwar, R. P.; Kitajima, M.; Nagao, T. Spectrally selective mid-infrared thermal emission from molybdenum plasmonic metamaterial operated up to 1000° C. *Advanced Optical Materials* **2016**, *4*, 1987–1992.

(20) Joulain, K.; Mulet, J.-P.; Marquier, F.; Carminati, R.; Greffet, J.-J. Surface electromagnetic waves thermally excited: Radiative heat transfer, coherence properties and Casimir forces revisited in the near field. *Surface Science Reports* **2005**, *57*, 59–112.

(21) Volokitin, A.; Persson, B. N. Near-field radiative heat transfer and noncontact friction. *Reviews of Modern Physics* **2007**, *79*, 1291.

(22) Krivanek, O. L.; Lovejoy, T. C.; Dellby, N.; Aoki, T.; Carpenter, R. W.; Rez, P.; Soignard, E.; Zhu, J.; Batson, P. E.; Lagos, M. J. et al. Vibrational spectroscopy in the electron microscope. *Nature* **2014**, *514*, 209–212.

(23) Lagos, M. J.; Bicket, I. C.; Mousavi M, S. S.; Botton, G. A. Advances in ultrahigh-energy resolution EELS: phonons, infrared plasmons and strongly coupled modes. *Microscopy* **2022**, *71*, i174–i199.

(24) Kumar, V.; Camden, J. P. Imaging vibrational excitations in the electron microscope. *The Journal of Physical Chemistry C* **2022**, *126*, 16919–16927.

(25) Lagos, M. J.; Batson, P. E. Thermometry with subnanometer resolution in the electron microscope using the principle of detailed balancing. *Nano Letters* **2018**, *18*, 4556–4563.

(26) Idrobo, J. C.; Lupini, A. R.; Feng, T.; Unocic, R. R.; Walden, F. S.; Gardiner, D. S.; Lovejoy, T. C.; Dellby, N.; Pantelides, S. T.; Krivanek, O. L. Temperature measurement by a nanoscale electron probe using energy gain and loss spectroscopy. *Physical Review Letters* **2018**, *120*, 095901.

(27) Liu, C.; Wu, Y.; Hu, Z.; Busche, J. A.; Beutler, E. K.; Montoni, N. P.; Moore, T. M.; Magel, G. A.; Camden, J. P.; Masiello, D. J. et al. Continuous wave resonant photon stimulated electron energy-gain and electron energy-loss spectroscopy of individual plasmonic nanoparticles. *ACS Photonics* **2019**, *6*, 2499–2508.

(28) Collette, R.; Garfinkel, D. A.; Hu, Z.; Masiello, D. J.; Rack, P. D. Near field excited state imaging via stimulated electron energy gain spectroscopy of localized surface plasmon resonances in plasmonic nanorod antennas. *Scientific Reports* **2020**, *10*, 12537.

(29) Bourgeois, M. R.; Nixon, A. G.; Chalifour, M.; Beutler, E. K.; Masiello, D. J. Polarization-Resolved Electron Energy Gain Nanospectroscopy With Phase-Structured Electron Beams. *Nano Letters* **2022**, *22*, 7158–7165.

(30) Das, P.; Blazit, J.; Tencé, M.; Zagonel, L.; Auad, Y.; Lee, Y.; Ling, X.; Losquin, A.; Colliex, C.; Stéphan, O. et al. Stimulated electron energy loss and gain in an electron microscope without a pulsed electron gun. *Ultramicroscopy* **2019**, *203*, 44–51.

(31) Bigelow, N. W.; Vaschillo, A.; Camden, J. P.; Masiello, D. J. Signatures of Fano Interferences in the Electron Energy Loss Spectroscopy and Cathodoluminescence of Symmetry-Broken Nanorod Dimers. *ACS Nano* **2013**, *7*, 4511–4519.

(32) Smith, K. C.; Olafsson, A.; Hu, X.; Quillin, S. C.; Idrobo, J. C.; Collette, R.; Rack, P. D.; Camden, J. P.; Masiello, D. J. Direct observation of infrared plasmonic Fano antiresonances by a nanoscale electron probe. *Physical Review Letters* **2019**, *123*, 177401.

(33) Baffou, G.; Girard, C.; Quidant, R. Mapping Heat Origin in Plasmonic Structures. *Phys. Rev. Lett.* **2010**, *104*, 136805.

(34) Bhattacharjee, U.; West, C. A.; Hosseini Jebeli, S. A.; Goldwyn, H. J.; Kong, X.-T.; Hu, Z.; Beutler, E. K.; Chang, W.-S.; Willets, K. A.; Link, S. et al. Active Far-Field Control of the Thermal Near-Field via Plasmon Hybridization. *ACS Nano* **2019**, *13*, 9655–9663.

(35) Hosseini Jebeli, S. A.; West, C. A.; Lee, S. A.; Goldwyn, H. J.; Bilchak, C. R.; Fakhraai, Z.; Willets, K. A.; Link, S.; Masiello, D. J. Wavelength-Dependent Photothermal Imaging Probes Nanoscale Temperature Differences among Subdiffraction Coupled Plasmonic Nanorods. *Nano Letters* **2021**, *21*, 5386–5393.

(36) Wu, Y.; Hu, Z.; Kong, X.-T.; Idrobo, J. C.; Nixon, A. G.; Rack, P. D.; Masiello, D. J.; Camden, J. P. Infrared plasmonics: STEM-EELS characterization of Fabry-Pérot resonance damping in gold nanowires. *Physical Review B* **2020**, *101*, 085409.

(37) Liberko, J. J.; Busche, J. A.; Seils, R.; Bechtel, H. A.; Rack, P. D.; Masiello, D. J.; Camden, J. P. Probing nanoparticle substrate interactions with synchrotron infrared

nanospectroscopy: Coupling gold nanorod Fabry-Pérot resonances with SiO_2 and h-BN phonons. *Physical Review B* **2021**, *104*, 035412.

(38) Aleshire, K.; Pavlovetc, I. M.; Collette, R.; Kong, X.-T.; Rack, P. D.; Zhang, S.; Masiello, D. J.; Camden, J. P.; Hartland, G. V.; Kuno, M. Far-field midinfrared super-resolution imaging and spectroscopy of single high aspect ratio gold nanowires. *Proc. Natl. Acad. Sci. U. S. A.* **2020**, *117*, 2288–2293.

(39) Ibach, H. Electron energy loss spectroscopy: the vibration spectroscopy of surfaces. *Surface Science* **1994**, *299*, 116–128.

(40) Joulain, K.; Carminati, R.; Mulet, J.-P.; Greffet, J.-J. Definition and measurement of the local density of electromagnetic states close to an interface. *Physical Review B* **2003**, *68*, 245405.

(41) Boudarham, G.; Kociak, M. Modal decompositions of the local electromagnetic density of states and spatially resolved electron energy loss probability in terms of geometric modes. *Physical Review B* **2012**, *85*, 245447.

(42) García de Abajo, F. J.; Kociak, M. Probing the photonic local density of states with electron energy loss spectroscopy. *Physical Review Letters* **2008**, *100*, 106804.

(43) Barnes, W. L.; Horsley, S. A.; Vos, W. L. Classical antennas, quantum emitters, and densities of optical states. *Journal of Optics* **2020**, *22*, 073501.

(44) Purcell, E. M.; Torrey, H. C.; Pound, R. V. Resonance absorption by nuclear magnetic moments in a solid. *Physical Review* **1946**, *69*, 37.

(45) Quillin, S. C.; Cherqui, C.; Montoni, N. P.; Li, G.; Camden, J. P.; Masiello, D. J. Imaging plasmon hybridization in metal nanoparticle aggregates with electron energy-loss spectroscopy. *Journal of Physical Chemistry C* **2016**, *120*, 20852–20859.

(46) Olafsson, A.; Khorasani, S.; Busche, J. A.; Araujo, J. J.; Idrobo, J. C.; Gamelin, D. R.; Masiello, D. J.; Camden, J. P. Imaging infrared plasmon hybridization in doped semiconductor nanocrystal dimers. *Journal of Physical Chemistry Letters* **2021**, *12*, 10270–10276.

(47) Pan, F.; Smith, K. C.; Nguyen, H. L.; Knapper, K. A.; Masiello, D. J.; Goldsmith, R. H. Elucidating energy pathways through simultaneous measurement of absorption and transmission in a coupled plasmonic–photonic cavity. *Nano Letters* **2019**, *20*, 50–58.

(48) Fussell, D.; McPhedran, R.; de Sterke, C. M. Decay rate and level shift in a circular dielectric waveguide. *Physical Review A* **2005**, *71*, 013815.

(49) Cherqui, C.; Li, G.; Busche, J. A.; Quillin, S. C.; Camden, J. P.; Masiello, D. J. Multipolar nanocube plasmon mode-mixing in finite substrates. *Journal of Physical Chemistry Letters* **2018**, *9*, 504–512.

(50) García de Abajo, F. J.; Kociak, M. Electron energy-gain spectroscopy. *New Journal of Physics* **2008**, *10*, 073035.

(51) García de Abajo, F. J. Optical excitations in electron microscopy. *Reviews of Modern Physics* **2010**, *82*, 209.

(52) Cherqui, C.; Thakkar, N.; Li, G.; Camden, J. P.; Masiello, D. J. Characterizing localized surface plasmons using electron energy-loss spectroscopy. *Annual Review of Physical Chemistry* **2016**, *67*, 331–357.

(53) Kischkat, J.; Peters, S.; Gruska, B.; Semtsiv, M.; Chashnikova, M.; Klinkmüller, M.; Fedosenko, O.; Machulik, S.; Aleksandrova, A.; Monastyrskyi, G. et al. Mid-infrared optical properties of thin films of aluminum oxide, titanium dioxide, silicon dioxide, aluminum nitride, and silicon nitride. *Applied Optics* **2012**, *51*, 6789–6798.

(54) Krasnok, A. E.; Slobozhanyuk, A. P.; Simovski, C. R.; Tretyakov, S. A.; Poddubny, A. N.; Miroshnichenko, A. E.; Kivshar, Y. S.; Belov, P. A. An antenna model for the Purcell effect. *Scientific Reports* **2015**, *5*, 12956.

TOC Graphic

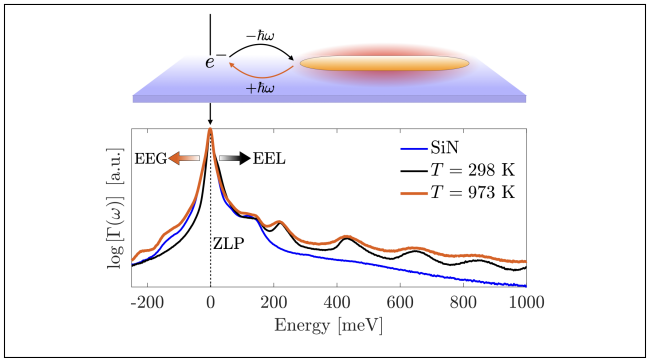
e^-
$-\hbar\omega$
$+\hbar\omega$
EEG
EEL
ZLP
SiN
$T = 298$ K
$T = 973$ K
$\log[\Gamma(\omega)]$ [a.u.]
-200
0
200
400
600
800
1000
Energy [meV]